Quantum chemical calculations show that the uranium molecule U2 has a quintuple bond

Gagliardi, Laura; Roos, Björn O.

However, an additional effect needs to be taken into account in our structure. E_{21} decreases at a far greater rate with increasing temperature than does $\hbar\omega_L$, because of the increased electric field required for the higher threshold current density and the large spatial separation of states 2 and 1. As a result, the 2–1 'diagonal' transition shifts to the red, via the linear Stark effect, much more than does the 7–6 'vertical' transition. The net effect is the observed blueshift of the Stokes emission. This behaviour therefore represents additional evidence that the emission at 9 μm cannot be due to ordinary laser action. □

Methods

Device

The growth started with a 0.7-μm-thick low n-doped ($n = 5 \times 10^{16}\,cm^{-3}$) GaInAs layer acting as lower waveguide core, on top of which the 30 repetitions of the active region and Raman structure periods (Fig. 1b) were grown. A 0.5 μm GaInAs layer ($n = 5 \times 10^{16}\,cm^{-3}$) completes the waveguide core, on top of which an AlInAs cladding layer was grown with a total thickness of 2 μm, where the first 1 μm was doped to $n = 1 \times 10^{17}\,cm^{-3}$, while the rest of it was doped to $n = 5 \times 10^{17}\,cm^{-3}$. The topmost layer was composed of a highly doped ($n = 4 \times 10^{18}\,cm^{-3}$) 0.8-μm-thick GaInAs layer for plasmon enhanced confinement, and a final 0.1-nm-thick GaInAs contact layer Sn-doped to $n = 1 \times 10^{20}\,cm^{-3}$. The material was processed into ridge waveguides 2.5 mm long and 14–20 μm wide, with a 350-nm-thick Si_3N_4 passivating layer on the lateral walls of the ridge and a Ti(30 nm)/Au(300 nm) top contact. A non-alloyed Ge/Au contact was deposited on the back. The samples were indium-soldered on Ni/Au plated copper holders and mounted in a liquid-nitrogen flow cryostat.

Measurements

A Fourier transform infrared spectrometer was used for optical measurements, together with a calibrated room-temperature HgCdTe detector for the optical power–current characterization. To filter out only the pump laser wavelength in order to measure the optical power emitted at the Stokes frequency, a long-wavelength ($\lambda > 7.5$ μm) pass filter was placed along the light path.

Received 3 September 2004; accepted 4 January 2005; doi:10.1038/nature03330.

1. Boyd, R. W. *Nonlinear Optics* (Academic, New York, 1992).
2. Shen, Y. R. *The Principles of Nonlinear Optics* (John Wiley & Sons, Hoboken, 1984).
3. Pask, H. M. The design and operation of solid-state Raman lasers. *Prog. Quant. Electron.* **27,** 3–56 (2003).
4. Nishizawa, J. & Suto, K. Semiconductor Raman laser. *J. Appl. Phys.* **51,** 2429–2431 (1980).
5. Grabtchikov, A. S. *et al.* All solid-state diode-pumped Raman laser with self-frequency conversion. *Appl. Phys. Lett.* **75,** 3742–3744 (1999).
6. Liu, H. C. *et al.* Intersubband Raman laser. *Appl. Phys. Lett.* **78,** 3580–3582 (2001).
7. Liu, H. C. *et al.* Coupled electron-phonon modes in optically pumped resonant intersubband lasers. *Phys. Rev. Lett.* **90,** 077402 (2003).
8. Spillane, S. M., Kippenberg, T. J. & Vahala, L. J. Ultralow-threshold Raman laser using a spherical dielectric microcavity. *Nature* **415,** 621–623 (2002).
9. Capasso, F., Sirtorí, C. & Cho, A. Y. Coupled quantum well semiconductors with giant electric field tunable nonlinear optical properties in the infrared. *IEEE J. Quant. Electron.* **30,** 1313–1326 (1994).
10. Rosencher, E. *et al.* Quantum engineering of optical nonlinearities. *Science* **271,** 168–173 (1996).
11. Owschimikow, N. *et al.* Resonant second-order nonlinear optical processes in quantum cascade lasers. *Phys. Rev. Lett.* **90,** 043902 (2003).
12. Gmachl, C. *et al.* Optimized second-harmonic generation in quantum cascade lasers. *IEEE J. Quant. Electron.* **39,** 1345–1355 (2003).
13. Bengloan, J.-Y. *et al.* Intracavity sum-frequency generation in GaAs quantum cascade lasers. *Appl. Phys. Lett.* **84,** 2019–2021 (2004).
14. Khurgin, J. B., Sun, G., Friedman, L. R. & Soref, R. A. Comparative analysis of optically pumped intersubband lasers and intersubband Raman oscillators. *J. Appl. Phys.* **78,** 7398–7400 (1995).
15. Faist, J., Hofstetter, D., Beck, M. & Aellen, T. Bound-to-continuum and two-phonon resonance, quantum-cascade lasers for high duty cycle, high-temperature operation. *IEEE J. Quant. Electron.* **38,** 533–546 (2002).
16. Capasso, F. *et al.* New frontiers in quantum cascade lasers and applications. *IEEE J. Select. Topics Quant. Electron.* **6,** 931–947 (2000).
17. Belyanin, A. A., Bentley, C., Capasso, F., Kocharovskaya, O. & Scully, M. O. Inversionless lasing with self-generated driving field. *Phys. Rev. A* **64,** 013814 (2001).
18. Kocharovskaya, O., Rostovtsev, Yu. V. & Imamoglu, A. Inversionless amplification in the three-level atoms with and without a hidden inversion in reservoir. *Phys. Rev. A* **58,** 649–654 (1998).
19. Gmachl, C. *et al.* Dependence of the device performance on the number of stages in quantum-cascade lasers. *IEEE J. Select. Topics Quant. Electron.* **5,** 808–816 (1999).
20. Helm, M. in *Intersubband Transitions in Quantum Wells: Physics and Applications I* (eds Liu, H. C. & Capasso, F.) 1–91 (Academic, London, 2000).

Acknowledgements We thank C. Gmachl for many discussions. A.B. acknowledges support from the TAMU TITF Initiative.

Competing interests statement The authors declare that they have no competing financial interests.

Correspondence and requests for materials should be addressed to M.T. (troccoli@deas.harvard.edu) or A. B. (belyanin@jewel.tamu.edu).

Quantum chemical calculations show that the uranium molecule U_2 has a quintuple bond

Laura Gagliardi* **& Björn O. Roos***

Dipartimento di Chimica Fisica "F. Accascina", Universita' degli Studi di Palermo, Viale delle Scienze – Parco d'Orleans II, I-90128 Palermo, Italy, and Department of Theoretical Chemistry, Chemical Center, POB 124, S-221 00 Lund, Sweden

* These authors contributed equally to this work

Covalent bonding is commonly described by Lewis's theory[1], with an electron pair shared between two atoms constituting one full bond. Beginning with the valence bond description[2] for the hydrogen molecule, quantum chemists have further explored the fundamental nature of the chemical bond for atoms throughout the periodic table, confirming that most molecules are indeed held together by one electron pair for each bond. But more complex binding may occur when large numbers of atomic orbitals can participate in bond formation. Such behaviour is common with transition metals. When involving heavy actinide elements, metal–metal bonds might prove particularly complicated. To date, evidence for actinide–actinide bonds is restricted to the matrix-isolation[3] of uranium hydrides, including H_2U–UH_2, and the gas-phase detection[4] and preliminary theoretical study[5] of the uranium molecule, U_2. Here we report quantum chemical calculations on U_2, showing that, although the strength of the U_2 bond is comparable to that of other multiple bonds between transition metals, the bonding pattern is unique. We find that the molecule contains three electron-pair bonds and four one-electron bonds (that is, 10 bonding electrons, corresponding to a quintuple bond), and two ferromagnetically coupled electrons localized on one U atom each—so all known covalent bonding types are contributing.

Multiple chemical bonds between transition metals were unknown to inorganic chemists until the crystal structure of $K_2[Re_2Cl_8]\cdot 2H_2O$ was reported[6] in 1965. A surprisingly short Re–Re distance of 2.24 Å was found, and assigned to a quadruple bond between the two rhenium atoms. Since then, hundreds of metal–metal multiple bonds have been characterized[7]. Here we extend the concept of metal–metal multiple bonding to the case of two actinide atoms.

The uranium atom (atomic number 92) has the ground-state electronic configuration $(5f)^3(6d)^1(7s)^2$, corresponding to a quintet ground state. However, the energy cost of unpairing the 7*s* electrons by forming hybrid orbitals is minimal, and uranium thus has in principle six electrons available with which to form chemical bonds. In a Lewis-like formalism, these electrons would combine as electron-pair bonds, giving rise to a hextuple bond between the two atoms and a singlet ground state. Such behaviour is seen with the chromium dimer[8], where the six valence electrons reside in the 3*d* and 4*s* orbitals of the Cr atom.

But whereas the Cr atom has exactly one valence electron in each of its six valence orbitals (the five 3*d* and one 4*s* orbitals), the U atom has 16 orbitals (seven 5*f*, five 6*d*, one 7*s* and three 7*p*) that are energetically close to one another. The bonding situation involving uranium is thus considerably more complex, given that all 16 orbitals may be considered valence orbitals available for forming the chemical bond in U_2. This complexity makes simple inferences regarding the nature and strength of the U_2 bond impossible, despite the fact that the strength of a covalent bond depends only on the energy of the atomic orbitals on the two different centres involved, and on the overlap between the orbitals. In the case of U_2, overlap between two 7*s* orbitals and between three out of the five 6*d*

orbitals (forming one σ-type and two π-type orbitals, respectively) will be large. The 5*f* orbitals will all have smaller overlap. However, the 5*f* atomic orbital energy level is lower than that of the 6*d* and 7*s* levels, and this would favour a system that does not deviate too much from the electronic configuration of the free atom when forming the dimer.

Given this complex situation, accurate computational investigations of the bonding in U_2 call for a method that allows all valence orbitals to combine freely to form the most stable chemical bond. The complete-active-space self-consistent-field (CASSCF) method[9] is such a method, offering maximum flexibility for describing electronic structures and capable of handling arbitrary spin. This flexibility is important because we cannot assume anything concerning the final number of paired electrons in U_2.

CASSCF was used to generate multireference wavefunctions for subsequent multiconfigurational second-order perturbation theory calculations of the dynamic correlation energy (CASPT2)[10]. The effects of relativity, which are substantial for atoms as heavy as uranium[11], were taken into account. The calculations were performed with MOLCAS-6.0 quantum chemical software[12] (see Methods for details).

Trial studies including different sets of valence orbitals in the active space all showed that three 'normal' electron-pair bonds are formed by hybrid atomic orbitals dominated by 7*s* and 6*d* character. Double occupation of these three orbitals was thus enforced in subsequent calculations. The remaining six electrons were then allowed to freely occupy the remaining 5*f* and 6*d* orbitals while searching for the occupation resulting in the lowest energy. The most stable electronic structure was found to be a septet state (that is, the remaining six electron spins are parallel), and to have a total orbital angular momentum, Λ, equal to 11 atomic units (a.u.).

The molecular orbitals involved in forming U_2 are depicted in Fig. 1, together with the occupation number of each orbital (or pair of orbitals). As illustrated in the figure, the lowest-energy doubly occupied molecular orbital is of $7s\sigma_g$ type, corresponding to a 'typical' single σ-bond. The other two doubly occupied orbitals are degenerate, of covalent π-type and result from combinations of 6*d* and 5*f* atomic orbitals ($6d\pi_u$ in the figure). Two singly occupied orbitals, of σ-type ($6d\sigma_g$) and δ-type ($6d\delta_g$), respectively, give rise to one-electron bonds between the two atoms. Two further singly occupied orbitals, of δ-type ($5f\delta_g$) and π-type ($5f\pi_u$), respectively, give rise to two additional (but weak) one-electron bonds. Finally, two electrons occupy what may be considered fully localized $5f\varphi$ orbitals. Overall, our calculations indicate that U_2 has three strong 'normal' electron-pair bonds, two fully developed one-electron bonds, two weak one-electron bonds, and two localized electrons. The singly occupied $5f\varphi$ orbitals add up to one 5*f* orbital on each atom with the electron spins parallel. In such a situation, the two electrons usually couple such that the total spin becomes zero (spin-up on one atom and spin-down on the other), because this antiferromagnetic coupling provides some additional bonding, even if small. For U_2, however, all spins are predicted to be parallel (ferromagnetic coupling), which can be attributed to 'exchange stabilization': if all open-shell electrons have the same spin, the interaction between the non-bonding 5*f* electrons and the two one-electron bonds is energetically more favourable than the antiferromagnetic coupling of the 5*f* electrons.

The total wavefunction for the ground state can be expressed as a linear combination dominated by essentially two electronic configurations:

$$\begin{aligned}\Psi = {} & 0.782(7s\sigma_g)^2(6d\pi_u)^4(6d\sigma_g)^1(6d\delta_g)^1(5f\delta_g)^1(5f\pi_u)^1 \\ & \times(5f\varphi_u)^1(5f\varphi_g)^1 \\ & + 0.596(7s\sigma_g)^2(6d\pi_u)^4(6d\sigma_g)^1(6d\delta_g)^1(5f\delta_u)^1(5f\pi_g)^1 \\ & \times(5f\varphi_u)^1(5f\varphi_g)^1 + \text{small terms} \end{aligned} \quad (1)$$

All the 7*s*, 6*d* and 5*f* orbitals contribute to this wavefunction. The orbitals in equation (1) have been labelled according to their angular momenta *l*: $l = 0$ as σ, $l = +1$ or -1 as π, $l = +2$ or -2 as δ, and $l = +3$ or -3 as φ, with those where *l* differs from zero being doubly degenerate. The total orbital angular momentum, Λ, is obtained as the sum of the angular momenta of each electron. The σ-orbitals give no contribution. The $6d\pi_u$ orbitals are occupied by four electrons (a closed shell), so the summed contribution of these electrons is also zero. The remaining orbitals are singly occupied, and the calculations show that all angular momenta have the same sign, which is in accordance with Hund's second rule. Inspection of

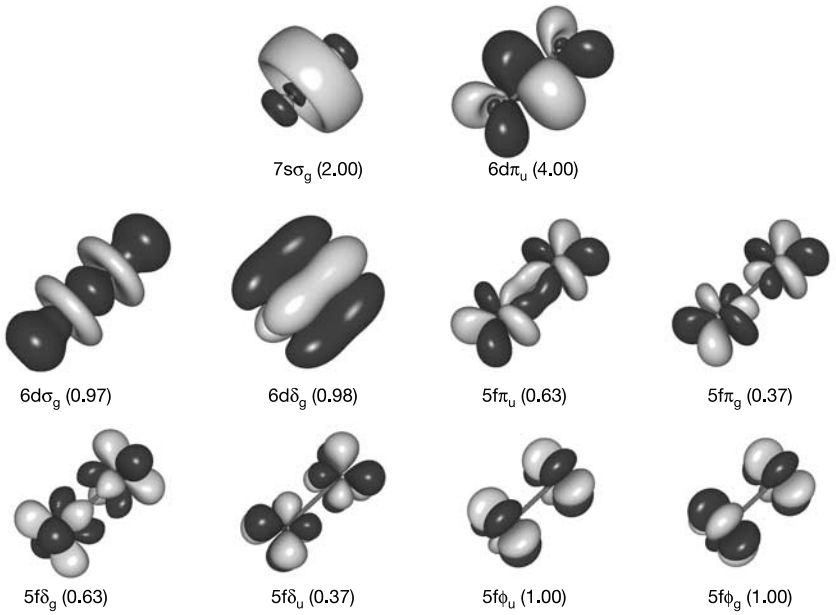

Figure 1 The active molecular orbitals forming the chemical bond between two uranium atoms. The orbital label is given below each orbital, together with the number of electrons occupying this orbital or pair of orbitals in the case of degeneracy.

the two terms in equation (1) then yields the total orbital angular momentum, $\Lambda = 0 + 2 + 2 + 1 + 3 + 3 = 11$. The calculations also show that all open shell electrons have parallel spin (Hund's first rule), resulting in a total spin angular momentum of 3, a septet state.

The U_2 chemical bond is thus more complex than any other known diatomic bond, with summation of the bonding electrons suggesting a quintuple bond. It is also unusual that strong bonding (see below) and strong ferromagnetism coexist as they do here. Moreover, its multi-radical nature (six electrons are available for binding) may support chemical bonds to a variety of ligands, such as in NU_2N or $Cl_3U_2Cl_3$. So far, the molecules OU_2O (ref. 4) and $H_2U_2H_2$ (ref. 3) have been detected.

The large number of orbitals available to the unpaired electrons permits this molecule to have the very large total orbital angular momentum of 11 a.u. However, in a heavy-atom system the combination of spin and orbital angular momenta must be considered. Our calculations show that in the case of U_2, the total angular momentum around the molecular axis is 14 a.u. (11 a.u. from the orbitals plus 3 a.u. from the total spin). High angular momentum values have been found in lanthanide compounds, where the 4*f* electrons giving rise to such high values are localized and do not participate in chemical bonding. In U_2, all electrons contribute to the bonding.

We have computed energies for a number of points in the neighbourhood of the equilibrium distance and also for two separated uranium atoms. The results for the distance with the lowest energy are presented in Table 1, giving energies where dynamic correlation is included in the calculations (CASPT2), and energies where both dynamic correlation and the effect of spin–orbit coupling are included in the calculations (CASPT2-SO). The CASPT2 level gives a dissociation energy of 40.2 kcal mol^{-1}, which decreases to 30.5 kcal mol^{-1} when the effect of spin–orbit coupling is added. We find an equilibrium bond distance of 2.43 Å and a harmonic vibrational frequency of 265 cm^{-1}. The only experimental datum on neutral U_2 available for comparison is a dissociation energy of 52 ± 5 kcal mol^{-1} (ref. 4). Spectroscopic studies are clearly desirable to assess our results and establish the ground electronic state of U_2, which is expected on the basis of the current work to be a $^7 11_{14}$ state. However, the present computational approach has been used in a number of earlier studies of actinide compounds, yielding results in agreement with experiment both for structural properties and relative energies (see, for example, the recent study[13] of the electronic spectrum of the UO_2 molecule). On the basis of the earlier results, we estimate that the computed U_2 bond distance is accurate to better than 0.05 Å. Estimating the uncertainty in the calculated binding energy is more difficult, because a comparably complicated chemical bond has not been treated before, and because balanced treatment of the molecule and the free atoms is difficult. Nonetheless, the U_2 molecule is undoubtedly bound with an appreciable binding energy. Moreover, the fact that all low-lying energy levels correspond to the same general electronic structure assures us that our description of the binding mechanism is correct.

The first attempt[5] to use correlated electronic structure theory to describe the bonding in a system as complex as U_2 faced methodological and computational limitations, so the calculations were not sufficiently accurate to fully describe the bonding. Moreover, spin-orbit effects were not explicitly included. In contrast, the present results have been obtained from a CASSCF wavefunction that is based on 20 active orbitals with six active electrons, which gives much greater flexibility in the construction of the most stable electronic structure with respect to the total spin and orbital angular momenta (see Methods for details). For example, while the earlier calculations on U_2 concluded correctly that six of the valence electrons occupy the $7s\sigma_g$ and the two $6d\pi_u$ orbitals, and that most of the binding energy is contained in these three chemical bonds, the use of only six active orbitals for the remaining six electrons resulted in a $^5\Sigma_g^+$ ground state unbound with respect to dissociation. The resultant suggestion that this state of U_2 will at most be a metastable species is very different from the present findings, but can be explained by the fact that the U_2 wavefunction exhibits strong configurational mixing not accounted for in the earlier work. This situation highlights the advantages of improved methodology and computational resources available today, which have made it possible for us to carry out an accurate computational investigation of a molecule as large as U_2 and reveal its unique bonding pattern. □

Table 1 **Calculated properties of U_2**

Property	CASPT2	CASPT2-SO
Total energy, $R = R_e$	−55,900.367918	−55,900.413591
Total energy, $R = R_\infty$	−55,900.299716	−55,900.364958
D_e (kcal mol^{-1})	40.2	30.5
R_e (Å)	2.43	2.43
ω_e (cm^{-1})	247	265

Total energy (atomic units) at the equilibrium bond distance, R_e, and at dissociation, R_∞, dissociation energy, D_e, equilibrium bond distance, R_e, and harmonic vibrational frequency, ω_e, for U_2 at the CASPT2 level and at the CASPT2 plus spin–orbit coupling (CASPT2-SO) level.

Methods

CASSCF calculations

The quantum chemical calculations were performed using the CASSCF method[9]. This is based on a partitioning of the molecular orbital space into three subspaces: inactive, active and external orbitals. The inactive orbitals are assumed to be doubly occupied. Remaining electrons occupy the active orbitals. The choice of these orbitals is crucial for the method. It should encompass all electronic structures that can be expected to be important for the quantum chemical problem studied. It is in principle simple to choose the active orbitals for the description of a chemical bond and its dissociation: one needs to use all orbitals that can be generated from the valence orbitals of the two atoms involved. It has been described above how the choice was made in the present case. We used a basis set of the atomic natural orbital (ANO) type that has been developed especially for relativistic calculations with the Douglas–Kroll–Hess (DKH) hamiltonian. A primitive set 26*s*23*p*17*d*13*f*5*g* was contracted to 9*s*8*p*7*d*5*f*2*g*. A larger ANO basis set was constructed for the calculation of the binding energy, in which the primitive set 27*s*24*p*18*d*14*f*6*g*3*h* was contracted to 11*s*10*p*8*d*6*f*3*g*1*h*.

CASPT2 and spin–orbit calculations

Dynamic correlation effects were computed using second-order perturbation theory (the CASPT2 method)[10]. For atoms as heavy as uranium it is necessary to include relativistic effects. They were included using the second-order DKH hamiltonian. The scalar part of this hamiltonian was used in the generation of the CASSCF wavefunction. The calculations were performed for a number of electronic states of *gerade* symmetry (after checking that states of *ungerade* symmetry were higher in energy). Spin–orbit (SO) coupling was then included by allowing the CASSCF wavefunctions to mix under the influence of the SO hamiltonian. The number of such wavefunctions was increased until the ground state energy was converged to 10^{-4} a.u. (1 a.u. = 2,625.50 kJ mol^{-1}). The final calculation included 16 CASSCF wavefunctions in the SO calculation. The method is described in detail in ref. 14, and references therein. It has been applied to a number of heavy atom systems with good results both for ground state properties and excited states.

Calculations were performed for a number of points around the equilibrium geometry. The binding energy was estimated from a calculation on the uranium atom, which was performed with the same basis set used for the U_2 molecule and with the valence orbitals active. In the atomic calculation, the full diatomic basis set was used to correct for the basis set superposition error. The ground state of the uranium atom is ^{5}L, which is 17-fold degenerate. Calculations were performed for all 17 components. We used the corresponding wavefunctions as the basis in a subsequent SO calculation of the $J = 6$ ground level. The results of these calculations are presented in Table 1 and discussed in the text.

Received 8 September; accepted 2 December 2004; doi:10.1038/nature03249.

1. Lewis, G. N. The atom and the molecule. *J. Am. Chem. Soc.* **38,** 762–786 (1916).
2. Heitler, W. & London, F. Wechselwirkung neutraler Atome und homöopolare Bindung nach der Quantenmechanik. *Z. Phys.* **44,** 455–472 (1927).
3. Souter, P. F., Kushto, G. P., Andrews, L. & Neurock, M. Experimental and theoretical evidence for the formation of several uranium hydride molecules. *J. Am. Chem. Soc.* **119,** 1682–1687 (1997).
4. Gorokhov, L. N., Emelyanov, A. M. & Khodeev, Y. S. Mass-spectroscopic investigation of stability of gaseous molecules of U_2O_2 and U_2. *High Temp.* **12,** 1156–1158 (1974).
5. Pepper, M. & Bursten, B. E. Ab initio studies of the electronic structure of the diuranium molecule. *J. Am. Chem. Soc.* **112,** 7803–7804 (1990).
6. Cotton, F. A. & Harris, C. B. The crystal and molecular structure of dipotassium octachlorodirhenate(III) dihydrate, $K_2[Re_2Cl_8]2H_2O$. *Inorg. Chem.* **4,** 330–333 (1965).

7. Cotton, F. A. & Walton, R. A. *Multiple Bonds between Metal Atoms* (Wiley & Sons, New York, 1982).
8. Roos, B. O. The ground state potential for the chromium dimer revisited. *Collect. Czech. Chem. Commun.* **68,** 265–274 (2003).
9. Roos, B. O. in *Advances in Chemical Physics; Ab Initio Methods in Quantum Chemistry – II* Ch. 69 (ed. Lawley, K. P.) 399–445 (Wiley & Sons, Chichester, 1987).
10. Andersson, K., Malmqvist, P.-Å., Roos, B. O., Sadlej, A. J. & Wolinski, K. J. Second-order perturbation theory with a CASSCF reference function. *Phys. Chem.* **94,** 5483–5488 (1990).
11. Pyykkö, P. Relativistic effects in structural chemistry. *Chem. Rev.* **88,** 563–594 (1988).
12. Karlström, G. *et al.* MOLCAS: a program package for computational chemistry. *Comput. Mater. Sci.* **28,** 222–239 (2003).
13. Gagliardi, L., Heaven, M. C., Wisborg Krogh, J. & Roos, B. O. The electronic spectrum of the UO_2 molecule. *J. Am. Chem. Soc.* (in the press).
14. Roos, B. O. & Malmqvist, P.-Å. Relativistic quantum chemistry–the multiconfigurational approach. *Phys. Chem. Chem. Phys.* **6,** 2919–2927 (2004).

Acknowledgements We thank P. Pyykkö and C. J. Cramer for comments on the manuscript, P.-Å. Malmqvist and B. E. Bursten for discussions, and V. Veryazov for graphical assistance. This work was partially supported by Ministero dell'Istruzione, dell'Università e della Ricerca (MIUR), the Swedish Research council (VR) and the Swedish Foundation for Strategic Research (SSF).

Competing interests statement The authors declare that they have no competing financial interests.

Correspondence and requests for materials should be addressed to L.G. (laura.gagliardi@unipa.it).

Lithospheric structure of the Rio Grande rift

David Wilson[1], Richard Aster[1], Michael West[2], James Ni[2], Steve Grand[3], Wei Gao[3], W. Scott Baldridge[4], Steve Semken[5] & Paresh Patel[3]

[1]*Department of Earth and Environmental Science and Geophysical Research Center, New Mexico Institute of Mining and Technology, Socorro, New Mexico 87801, USA*
[2]*Department of Physics, New Mexico State University, Las Cruces, New Mexico 88003, USA*
[3]*Jackson School of Geosciences, University of Texas, Austin, Texas 78712, USA*
[4]*Earth and Environmental Sciences Division, MS D462, Los Alamos National Laboratory, Los Alamos, New Mexico 87545, USA*
[5]*Department of Geological Sciences, Arizona State University, Tempe, Arizona 85287, USA*

A high-resolution, regional passive seismic experiment[1–6] in the Rio Grande rift region of the southwestern United States has produced new images of upper-mantle velocity structure and crust–mantle topography. Synthesizing these results with geochemical[7–9] and other geophysical[10–13] evidence reveals highly symmetric lower-crustal and upper-mantle lithosphere extensional deformation, suggesting a pure-shear rifting mechanism for the Rio Grande rift. Extension in the lower crust is distributed over a region four times the width of the rift's surface expression. Here we propose that the laterally distributed, pure shear extension is a combined effect of low strain rate and a regionally elevated geotherm, possibly abetted by pre-existing lithospheric structures, at the time of rift initiation. Distributed extension in the lower crust and mantle has induced less concentrated vertical mantle upwelling and less vigorous small-scale convection[14] than would have arisen from more localized deformation. This lack of highly focused mantle upwelling may explain a deficit of rift-related volcanics in the Rio Grande rift compared to other major rift systems such as the Kenya rift[15,16].

Rifting has a profound influence on continental evolution, fundamentally controlling crustal thinning and continental breakup. The character of a continental rift depends on how lithospheric strain is accommodated. Possible strain configurations range between pure-shear and simple-shear end members. The pure-shear model is characterized by ductile deformation of the lower crust and mantle lithosphere and predicts symmetric thinning and a symmetric lithospheric cross-section with respect to the rift axis[17]. The simple-shear model is characterized by strain localization along a master or a sequence of low-angle (10° to 30° dip) detachment(s) that may span the entire lithosphere[18]. A low-angle detachment predicts an asymmetric lithospheric cross-section, with the greatest crustal thinning laterally offset from greatest mantle lithosphere thinning.

In both the simple-shear and the pure-shear models, extensional thinning of crust and mantle lithosphere produces local upwelling of warm asthenosphere to replace thinned lithosphere. Additional heat is released by adiabatic decompression, producing partial melting and rift-associated volcanism. The emplacement of advected warmer material creates lateral temperature gradients that can induce small-scale convection[19,20]. Small-scale convective cells may create significant additional horizontal stresses that further advance rifting, volcanism and other lithosphere-scale deformation[14,20].

The simple-shear and pure-shear models offer distinct topographic, heat flow, gravity anomaly, and lithospheric velocity structural predictions. Ideally, it should be possible to distinguish between the models by the topographic expression of the rift, because the asymmetry of simple-shear deformation predicts asymmetry in the flexural uplift of the rift flanks[21], with the greatest uplift offset laterally from the surface expression of the rift. Rift-flank topography along the Rio Grande rift (RGR) (Fig. 1) is in fact relatively symmetric about the rift axis, with variations of typically less than 1–2 km between opposing rift flanks. However, the use of topography as a diagnostic tool may be significantly complicated by crustal composition and the fact that rifting has resulted in brittle deformation in the uppermost crust—expressed as a series of asymmetric grabens[15,22].

Similarly, the asymmetry of the simple-shear model predicts a complementary heat-flow asymmetry[23]. Heat-flow measurements in the RGR region show a broad region of roughly symmetric high heat flow trending approximately along the rift axis[24], consistent with pure-shear extension. However, regional heat-flow values along the RGR and elsewhere may be significantly complicated by advective hydrothermal transport within the crust.

One method of assessing the existence of simple-shear detachment(s) is to image the symmetry and location of maximum crustal thinning relative to the surface expression of the rift axis. We have constructed a new image of the crust–mantle boundary using receiver functions computed from teleseismic body waves recorded by the 950-km-long, 54-station LA RISTRA experiment[1–6], a linear transect that crossed the RGR obliquely near 34.5° (Fig. 1). Receiver function processing isolates P-to-S converted seismic phases generated by impedance discontinuities[25]. Discontinuity images are constructed by migration and stacking of many receiver functions with different ray paths through the crust and mantle, recorded at many stations. LA RISTRA receiver function images (Fig. 2) indicate crustal thickness ranging from 45 to 50 km beneath both the Colorado Plateau (stations NM34–UT54), and the Great Plains (TX01–NM20), with a rift-associated thinning to approximately 37 km centred beneath the RGR axis to within a few kilometres. These estimated crustal thicknesses are consistent with previous compilations of refraction surveys[26] across the RGR.

Using geologic constraints from previous seismic reflection work[24], we modelled the predicted geometry of the base of the crust (Moho) and the base of the lithosphere resulting from the amount of extension seen at the surface in the southern Albuquerque–Belen basin (16.9 km of extension over 60 km) (Figs 2, 3). The modelling technique[21] takes into account the kinematics of lithospheric extension, the isostatic response to crust and lithospheric thinning, and the elastic response of the lithosphere (flexure). Extension by either east- or west-dipping simple shear (Fig. 2a, b) predicts offset Moho upwarping that is